

Article

Mechanical Properties and Thermal Shock Performance of High-Energy-Rate-Forged W-1%TaC Alloy

Fan Feng ^{1,*}, Youyun Lian ¹, Jianbao Wang ¹, Jiupeng Song ^{2,3}, Binyou Yan ² and Xiang Liu ¹

¹ Fusion Science Center, Southwestern Institute of Physics, Chengdu 610225, China; lianny@swip.ac.cn (Y.L.); wangjb@swip.ac.cn (J.W.); xliu@swip.ac.cn (X.L.)

² China National R&D Center for Tungsten Technology, Xiamen Tungsten Co., Ltd., Xiamen 361000, China; jpsong@swip.ac.cn (J.S.); yanbinyou@cxtc.com (B.Y.)

³ School of Materials Science and Engineering, Xihua University, Chengdu 610039, China

* Correspondence: fengf@swip.ac.cn; Tel.: +86-134-5868-5594

Abstract: Tungsten is a metal with a high melting point and thermal conductivity, but its inherent brittleness limits its application in the industry. Dispersion strengthening and plastic deformation are considered to be an effective means to improve the properties of tungsten alloys. In this work, the mechanical properties and thermal shock performance of W-1% TaC alloy prepared by hot pressing followed by high-energy-rate forging (HERFing) and annealing treatment were investigated. The microstructure of the tungsten material was characterized via metallography, scanning electron microscopy and electron backscattering diffraction imaging. The mechanical properties were studied by tensile testing. The thermal shock performance of the HERFed W-TaC was evaluated using an electron beam device. The forged tungsten possessed a disc-shaped grain structure. The forged W-TaC alloy exhibited a good mechanical performance at an elevated temperature, which was different from the response of other tungsten alloys. The HERFing process effectively increased the cracking threshold of W-TaC alloy under electron beam transient thermal load. The lamellar grain structure of the forged tungsten material prevented cracks from propagating deeply into the material.

Keywords: tungsten materials; high-energy-rate-forge; mechanical properties; thermal load



Citation: Feng, F.; Lian, Y.; Wang, J.; Song, J.; Yan, B.; Liu, X. Mechanical Properties and Thermal Shock Performance of High-Energy-Rate-Forged W-1%TaC Alloy. *Crystals* **2022**, *12*, 1047. <https://doi.org/10.3390/cryst12081047>

Academic Editor: Sergio Brutti

Received: 5 July 2022

Accepted: 24 July 2022

Published: 28 July 2022

Publisher's Note: MDPI stays neutral with regard to jurisdictional claims in published maps and institutional affiliations.



Copyright: © 2022 by the authors. Licensee MDPI, Basel, Switzerland. This article is an open access article distributed under the terms and conditions of the Creative Commons Attribution (CC BY) license (<https://creativecommons.org/licenses/by/4.0/>).

1. Introduction

Tungsten and tungsten-based alloys are attracting a growing amount of interest for their use as functional and structural materials in advanced nuclear facilities [1–4]. Tungsten is a promising plasma-facing material for fusion reactor divertors because of its high melting temperature, high thermal conductivity, low tritium retention, and low sputtering yield [5–8]. The International Thermonuclear Experimental Reactor Organization decided to use a full tungsten divertor from the beginning of operation [9]. The divertor is designed to exhaust heat and particle fluxes. Inside the fusion device, the divertor faces three major challenges: neutron irradiation, ion irradiation, and high heat flux load. Currently, pure commercial tungsten exhibits low ductility, high ductile–brittle transition temperature (>400 °C), low recrystallization temperature (~1300 °C), and embrittlement due to recrystallization and irradiation [10–12]. These inherent disadvantages could be a big problem for the safe operation of future fusion reactors.

Several studies have recently attempted to combat the disadvantages of tungsten-based alloys. The performance of tungsten materials can be enhanced in terms of their composition and thermo-plastic processing. Micro-alloy and dispersion strengthening have been widely used in the preparation of tungsten alloy materials to enhance their composition. Tungsten–rhenium alloys can achieve room temperature (RT) ductility and promising machining capabilities [13]. Tungsten alloys strengthened by the dispersion of rare earth oxides, such as La₂O₃ and Y₂O₃, have been prepared by powder metallurgy methods; oxides can effectively inhibit grain growth and reduce grain size [14–18]. Rotary-forged

W-1% Y_2O_3 can obtain certain ductility at 250 °C, which is approximately 100 °C and 250 °C lower than those of SPSd + ball-milled and SPSed + sol-gel W-1% Y_2O_3 , respectively [19]. The addition of trace carbides, such as TiC [20] and ZrC [21], can also refine the grains and achieve good mechanical performance and low temperature ductility. In terms of the thermo-plastic processing of tungsten materials, swaging and rolling methods can be used for industrial applications. High-energy-rate forging (HERFing) is also an effective thermo-plastic processing technology used to engineer the properties of copper and 304 L stainless steel [22]. Lian [23] prepared the W- Y_2O_3 alloy with a certain ductility at 100 °C and good tensile strength via this technology.

In the present work, a bulk tungsten alloy was prepared by carbide dispersion strengthening in powder metallurgy and thermo-plastic deformation processing. Bulk W-1.0wt% TaC alloy was fabricated through mechanical alloying, hot pressing, and HERFing. W-TaC alloy undergoes severe plastic deformation during the HERFing process, and elongated grains and deformed texture can be obtained in the deformed samples. The effects of working processes and carbide addition on the microstructure, mechanical properties, and thermal shock performance of the W-TaC samples were explored.

2. Materials and Methods

W-1wt% TaC (WTC) alloys were prepared with pure tungsten (purity > 99.999%, average particle size of 2.5 μm , Xiamen Tungsten Co., Ltd., Xiamen, China) and nanosized TaC powders (average particle size 100 nm, purity > 99.9%, ZhongNuo Advanced Material Technology Co., Ltd., Beijing, China). The powders were ball milled by a planetary ball mill in an argon atmosphere at a ball-to-powder weight ratio of 6:1 and at 175 rpm for 10 h. Tungsten carbide balls were used to minimize impurity contamination. The milled powders were sintered at 1800 °C under a pressure of 30 MPa for 1 h in a vacuum furnace to yield sintered bulks. The hot-pressed WTC obtained was heated to 1550 °C and forged by HERFing with one pass into a disc with a height of 7 mm (from an initial cylinder with 25 mm height and 30 mm diameter), as displayed in Figure 1. Finally, the forged WTC disc was annealed at 1100 °C for 30 min to release thermal stress.

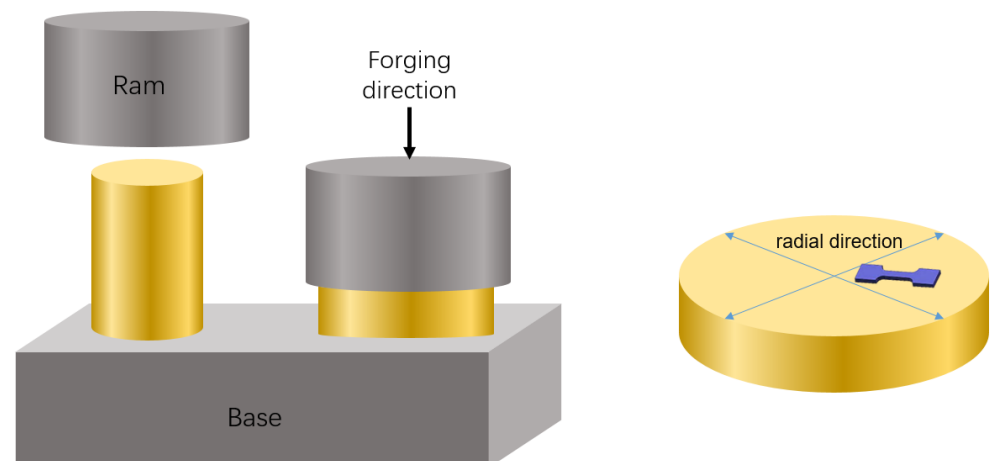


Figure 1. A schematic diagram showing the HERF process, and a tensile specimen cut from the forged disc.

Tensile properties were investigated via tensile tests along the diameter direction with an Instron-5967 device from RT to 600 °C in air at a strain rate of $2 \times 10^{-4} \text{ s}^{-1}$. Dog-bone-shaped specimens with a working length of 5 mm and a rectangular cross-section of 1.5 mm \times 1.0 mm were cut from the forged disc. The testing samples were mechanically polished with SiC abrasive paper. At least two to three samples were tested for each temperature to ensure repeatability.

Edge Localized Mode (ELM) transient thermal loads simulated the electron beam device EMS-60 (60 kW Electron Beam Material Test Scenario) installed at the Southwestern

Institute of Physics [24]. An electron beam was extracted from a tungsten cathode with an acceleration voltage of 120 KV. The beam was scanned across the surface with a high frequency of 37 kHz in the x-direction and 27 kHz in the y-direction. The power absorption coefficient is closely related to the type of material [25]. In the current study, a power absorption coefficient of 0.46 was determined using absorbed current measurements [26]. The dimensions of samples were 10 mm × 10 mm × 2.0 mm, and the loading area was approximately 4 mm × 4 mm. All test samples suffered 100 cycles with 1 ms pulse duration, and three different absorbed power densities of 220, 330, and 440 MW/m² were used. The surface morphology changes of the sintered and forged samples that underwent electron beam thermal loading were investigated.

The densities of the WTC samples were determined with the Archimedes method. The hardness measurements were carried out at RT using a Vickers hardness tester with a load of 5000 g and a dwell time of 15 s. Each sample was measured at least five times and averaged. Field-emission scanning electron microscopy was used to image the fracture surfaces of the WTC samples and their surface morphologies after electron beam thermal loading. The preferred orientation of the grains of forged WTC samples was studied with an electron backscatter diffraction (EBSD, Oxford Instruments Nanotechnology Tools Ltd., High Wycombe, UK) system. Tungsten grain size distribution and misorientation angle were also obtained by EBSD technology.

3. Results and Discussion

The relative density, Vickers hardness, and grain size of WTC alloys with different working processes are listed in Table 1. The HERFing process remarkably increased the relative density and Vickers hardness of the WTC alloy. The WTC materials' approximate relative density of 99.2% was achieved through HERFing. The Vickers hardness of the HERFed WTC sample was 552 HV, which was higher than that of the hot-pressed WTC sample. Metallographic analyses, which are shown in Figure 2, indicated that the WTC grains show evident changes after HERFing. The grain shape of the sintered WTC alloy was nearly equiaxial with a grain size of 3.74 μm, as shown in Figure 2a. After forging, the WTC alloy presents a lamellar structure and the grains are in a large disc shape, as shown in Figure 2b–d. These results may be due to recrystallization during HERFing resulting from high forging temperature (1550 °C), which differed from the result of the HERFed W-Y₂O₃ alloy [23].

Table 1. Working process, relative density, and hardness of the WTC alloy.

Working Process	Relative Density	Hardness/Hv	Average Grain Size/μm
Hot pressing	96.8%	436	3.74
HERFing	99.2%	552	–

The fracture surfaces of the as-forged and as-sintered WTC samples at RT observed with SEM are shown in Figure 3a,b. The fracture modes of the as-forged and as-sintered samples are markedly different. The forged and sintered samples are essentially ruptured in transgranular cleavage and intergranular fracture modes, respectively. The grain shape of the forged WTC specimen presents a long strip shape, whereas the equiaxed grains are dominant to the sintered specimen. Given that second-phase particles in tungsten alloy play a very important role, tungsten matrix should be inspected for the existence of TaC particles. The EDS results shown in Figure 3c demonstrate the presence of TaC particles. The red arrows in Figure 3a indicate the positions of some TaC particles in the tungsten matrix.

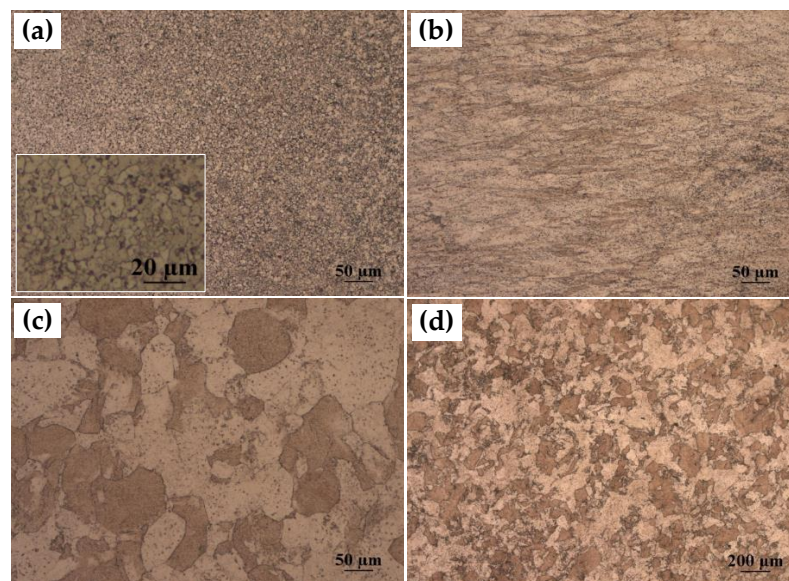


Figure 2. Metallograph of the hot-pressed WTC (a), thickness direction of HERFed WTC (b), and radial direction of HERFed WTC (c,d).

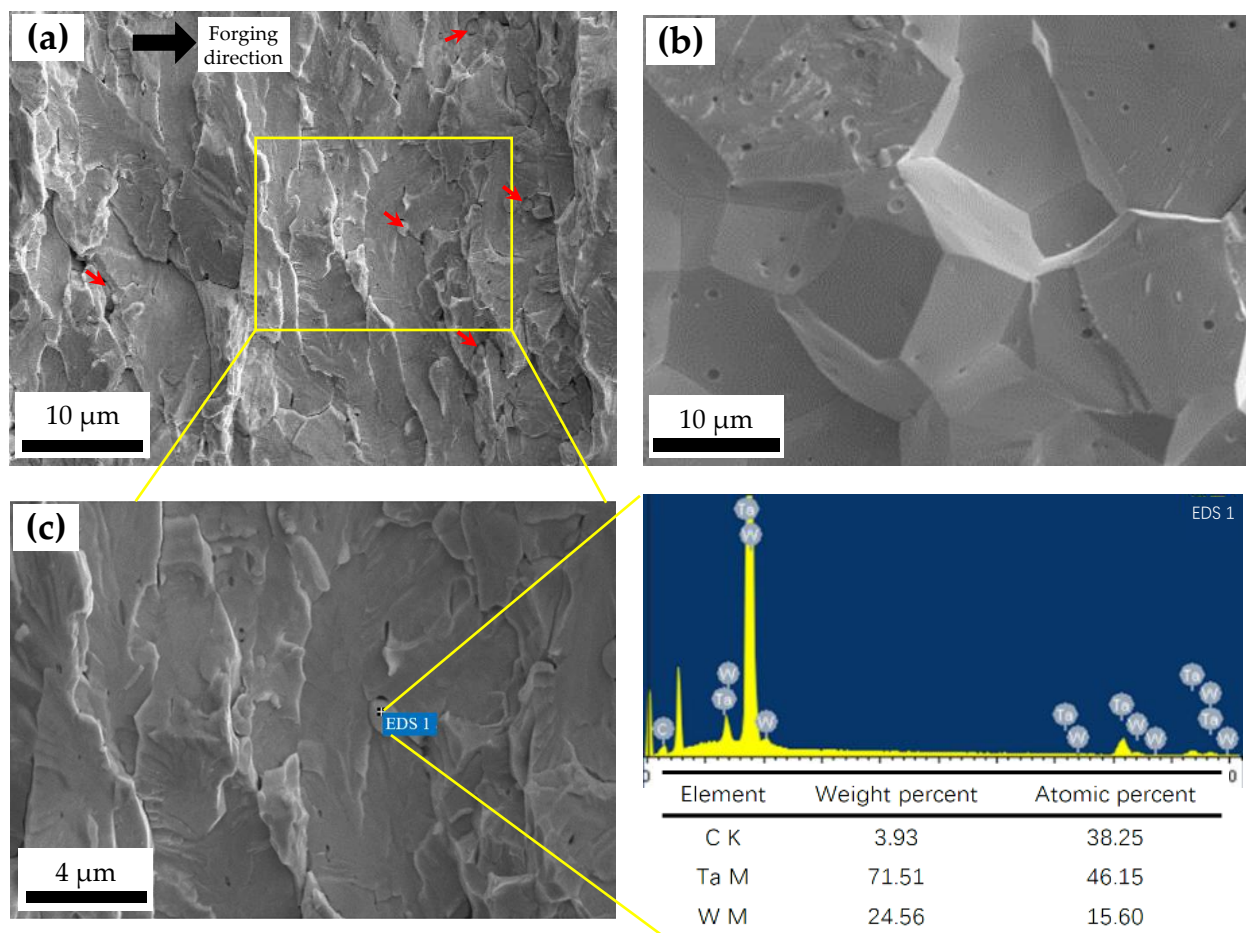


Figure 3. Tensile fracture of an as-forged WTC sample (a) and an as-sintered sample (b) at RT, black arrow shows the forging direction, and red arrows show TaC particles. (c) is an enlarged view of the yellow box in (a), it shows the TaC particle in tungsten matrix.

The tensile results of the forged WTC material from RT to 600 °C are presented in Figure 4a. The forged WTC alloy showed a typical brittle fracture from RT to 400 °C. Evident plastic deformation was detected when the temperature increased to 500 °C. The ultimate tensile strength and total elongation of the HERFed WTC alloy at 500 °C were 1001 MPa and 5.4%, respectively. The ultimate tensile strength of the forged WTC alloy is shown as a function of the test temperature in Figure 4b. The results of swaged W-Y₂O₃ [27], HERFed W-Y₂O₃ [23], rolled W-ZrC [21], and rolled W [28] are also presented for comparison. To some extent, the strength of forged WTC alloy increased with the test temperature. However, the strength of other reported tungsten materials decreased with increasing temperature. These materials showed the opposite trend. The strength of the WTC alloy exceeded those of other tungsten materials at 300 °C. Furthermore, with increasing temperature, the difference in strength increased. This result implied the good mechanical performance of forged WTC alloy at elevated temperatures.

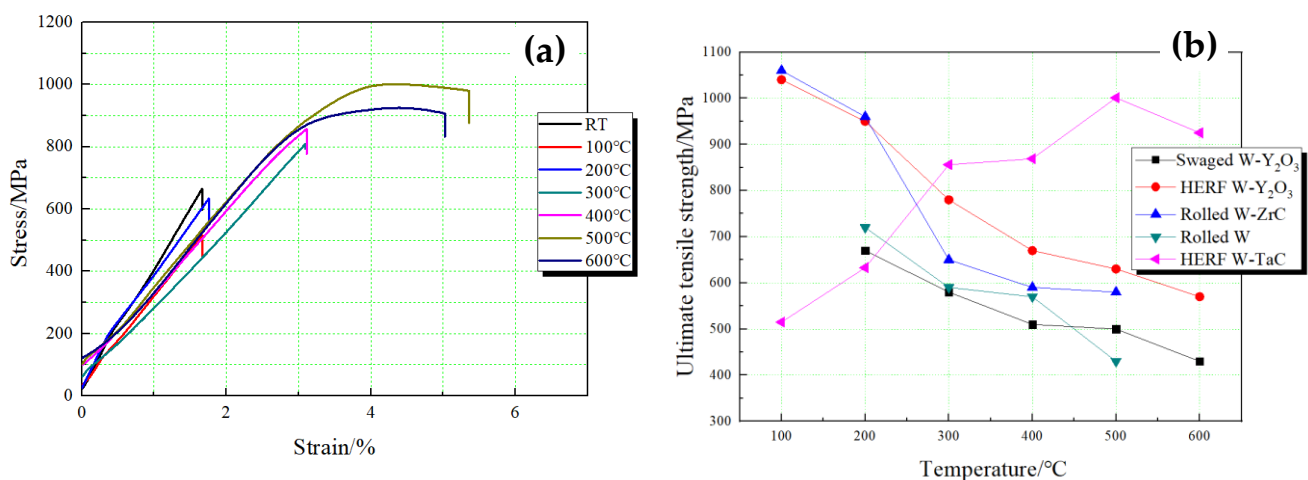


Figure 4. Tensile behaviors of forged WTC alloy (a) and the strength of some materials at different temperatures for comparison (b). Strength variation of swaged W-Y₂O₃ [27], HERFed W-Y₂O₃ [23], rolled W-ZrC [21], rolled W [28], and WTC at different temperatures.

It is well known that the microstructure of materials is closely related to their mechanical properties. Thus, microstructures should be intensively studied. The grain structure and texture of the HERFed WTC material were investigated by EBSD analysis. Figure 5 shows the microstructure of the HERFed WTC material. The green and black lines in Figure 5a indicate the low-angle grain boundaries (LAGBs, <15°) and high-angle grain boundaries (HAGBs, >15°) respectively. Dislocations are generated inside the grains under the effect of strain. With the accumulation of strain, dislocation density increased, and LAGBs were formed. The photograph is filled with numerous green lines, which indicated that a large number of dislocations were present inside the material. Figure 5b shows the distribution of the grain boundary misorientation angle. The fractions of LAGBs and HAGBs were 0.823 and 0.177, respectively. The distribution of grain boundary orientation (Correlated) and Mackenzie curve (Random) based on the random distribution of grain orientation largely differed, indicating that most of the grain boundaries are subgrain boundaries of low energy. In deformed materials, a single grain is generally defined only when the misorientation angle of the grain is greater than 15°. Otherwise, it is a subgrain. The grains with misorientation angles $\theta > 15^\circ$ were measured and calculated (Figure 5d). The average grain size is 4.99 μm . Quantitative analysis of the grain size distribution reveals a bimodal size distribution with two maxima: one <5 μm and the other >10 μm . Intuitively, Figure 5a also shows the bimodal size distribution of the WTC material. This lamellar bimodal structure may be the key of high mechanical strength. It has been reported that the heterogeneous structure can make dislocations pile up and accumulate to enhance back-stress hardening and dislocation hardening [29]. At the same time, the elongated

grains sandwiched between fine grains can produce high strain hardening [30]. These hardening effects combined with coarse grains with better stability at high temperature make the WTC alloy possess better high temperature strength than other tungsten materials.

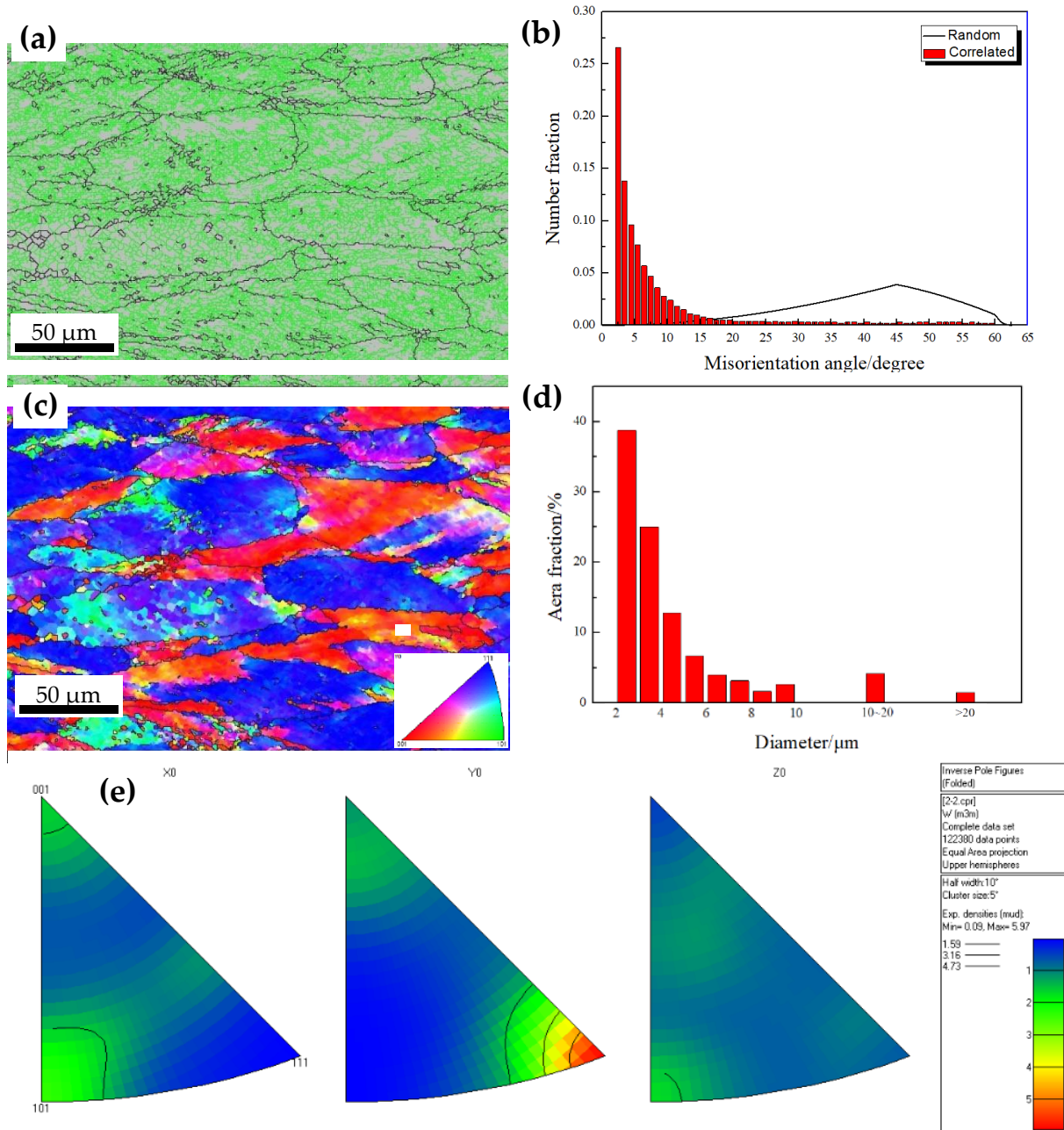


Figure 5. EBSD results of the HERFed WTC material. (a) Distribution of grain–subgrain boundary. (b) Misorientation distribution. (c) IPF mapping in the forging direction. (d) Grain size distribution. (e) Inverse pole figures.

Inverse pole figure (IPF) mapping and IPFs are shown in Figure 5c,e. The data were obtained from the cross-sectional plane parallel to the forging axis. In HERFing, a disc-shaped material has only two directions, namely, forging and radial. In Figure 5e, Y0 is the forging direction, and X0 and Z0 are the radial directions. As indicated in IPFs, the forged WTC material displays a strong $\langle 111 \rangle$ texture with a maximum intensity of 5.97 times random, which indicates a remarkable preferred orientation.

In future fusion devices, ELM transient events are inevitable during normal operation in the H-mode. Thus, transient thermal load resistance is very important for the performance of tungsten materials. To examine the response to transient thermal loading of WTC alloy, we conducted ELM-like thermal load tests upon hot-pressed and HERFed WTC samples at room temperature and adopted three absorbed power densities (220, 330, and 440 MW/m²). The surface morphologies of these samples exposed to the electron beam are displayed in Figure 6. The surface morphology of the two samples with ELM-like thermal load remains unchanged at 220 MW/m². With exposure to 330 MW/m², the sintered sample sustains cracks, and the forged one merely exhibits slight plastic deformation. As the absorbed power densities are increased to 440 MW/m², cracks appear in both samples. The surface of the forged sample is darker than that of the sintered one, which indicates that the degree of plastic deformation of the forged sample is greater than that of the sintered one. This result is due to the plastic deformation that caused the surface to roughen. The diffusion of the reflection of light due to the rough surface caused the sample surface to appear dark.

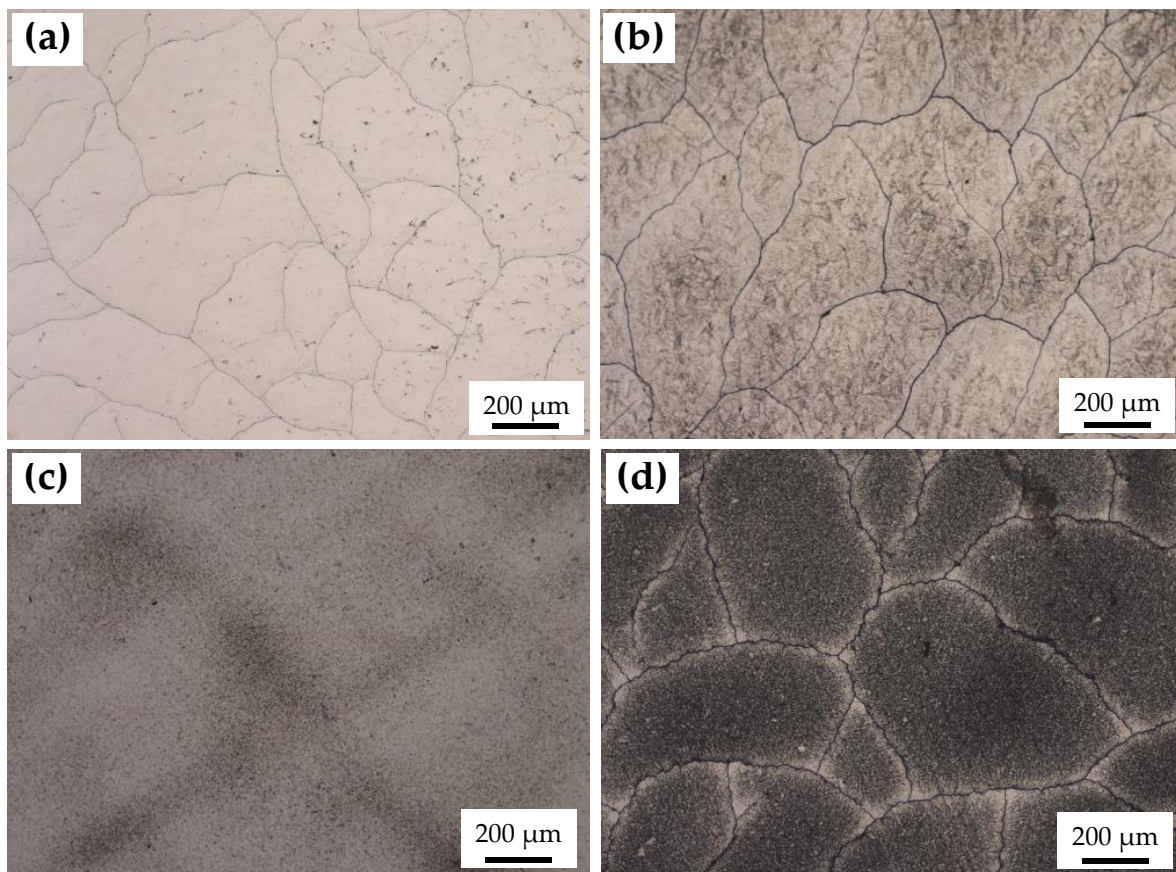


Figure 6. Surface morphologies of the WTC samples after ELM-like thermal loading. (a) As-sintered at 330 MW/m²; (b) As-sintered at 440 MW/m²; (c) As-forged at 330 MW/m²; (d) as-forged at 440 MW/m².

After thermal load tests, further information of the cracks under the surface is obtained by examining cross-section images. The light images of the cross-section of the WTC samples after thermal load are displayed in Figure 7. Figure 7a–c show the crack depth distribution of the as-sintered sample exposed to 330 MW/m² thermal load, the as-sintered sample exposed to 440 MW/m² thermal load, and the as-forged sample exposed to 440 MW/m² thermal load, respectively. The crack depth distribution of the three samples is different. The crack depth shown in Figure 7a is different, while the crack depths in Figure 7b are almost the same, and the crack depths in Figure 7c are also almost the same.



Figure 7. Light micrographs of the cross section of WTC samples after thermal loading. (a) As-sintered at 330 MW/m², (b) as-sintered at 440 MW/m², and (c) as-forged at 440 MW/m². The scale indicated is the same for all graphs.

Figure 8 shows the arithmetic mean depth of the major cracks. The crack depth of sample 2 was deeper than that of sample 1, and the depth was relatively uniform. This result was due to the larger absorbed power density of sample 2 compared with sample 1. Under the same absorbed power density, the crack depth of sample 3 was much lower than that of sample 2 and even lower than that of sample 1. This finding was due to the lamellar grain structure of forged tungsten material, which prevented the cracks from further propagating into the material.

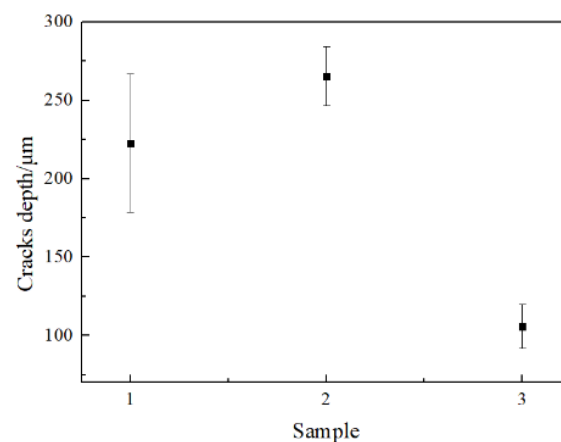


Figure 8. Comparison of the arithmetic mean depth of cracks after ELM-like thermal loading; 1, 2, and 3 represent the as-sintered sample with 330 MW/m² thermal load, the as-sintered sample with 440 MW/m² thermal load, and the as-forged sample with 440 MW/m² thermal load.

4. Conclusions

A tungsten material strengthened by TaC dispersion was prepared by hot pressing and subsequent HERFing. The mechanical properties, microstructures, and thermal shock performances were studied. Relative to the hot-pressed samples, the WTC alloy that underwent plastic deformation showed remarkably increased density and hardness. After HERFing, the WTC grains changed from equiaxed grains to disc-shaped grains. To some extent, the strength of the forged WTC alloy increased with testing temperature, which was markedly different from the response of other tungsten-based materials, including swaged/forged/rolled pure W and W-Y₂O₃ and W-ZrC composites. The thermal load test showed that the plastic deformed WTC material exhibited good resistance to thermal shock under ELM-like loads. The addition of carbide particles could improve the high-temperature mechanical properties. In addition, the thermal load tests showed that HERFing effectively improved the ductility of tungsten.

Author Contributions: Conceptualization, F.F. and Y.L.; methodology, F.F.; validation, F.F.; formal analysis, F.F.; investigation, F.F.; resources, F.F. and J.S.; data curation, F.F., B.Y. and J.W.; writing—original draft preparation, F.F.; writing—review and editing, Y.L.; visualization, F.F.; supervision, X.L.; project administration, Y.L.; funding acquisition, Y.L. and X.L. All authors have read and agreed to the published version of the manuscript.

Funding: This research was supported by the National Natural Science Foundation of China (Grant Nos. 11975092 and 11605044), 2020 CNNC Elite Project (Grant No. JZYF-2020-01) and Innovation Research of SWIP (Grant No. 202001XWCXRZ002).

Data Availability Statement: Not applicable.

Conflicts of Interest: The authors declare no conflict of interest.

References

1. Rieth, M.; Dudarev, S.L.; de Vicente, S.M.G.; Aktaa, J.; Ahlgren, T.; Antusch, S.; Armstrong, D.E.J.; Balden, M.; Baluc, N.; Barthe, M.F.; et al. Recent progress in research on tungsten materials for nuclear fusion applications in Europe. *J. Nucl. Mater.* **2013**, *432*, 482–500. [[CrossRef](#)]
2. Kawai, M.; Kurishita, H.; Kokawa, H.; Watanabe, S.; Sakaguchi, N.; Kikuchi, K.; Saito, S.; Yoshiie, T.; Iwase, H.; Ito, T.; et al. Development of advanced materials for spallation neutron sources and radiation damage simulation based on multi-scale models. *J. Nucl. Mater.* **2011**, *431*, 16–25. [[CrossRef](#)]
3. Ueda, Y.; Lee, H.T.; Ohno, N.; Kajita, S.; Kimura, A.; Kasada, R.; Nagasaka, T.; Hatano, Y.; Hasegawa, A.; Kurishita, H.; et al. Recent progress of tungsten R&D for fusion application in Japan. *Phys. Scr.* **2011**, *T145*, 014029. [[CrossRef](#)]
4. McManamy, T.; Rennich, M.; Gallmeier, F.; Ferguson, P.; Janney, J. 3MW solid rotating target design. *J. Nucl. Mater.* **2010**, *398*, 35–42. [[CrossRef](#)]
5. Reiser, J.; Rieth, M.; Dafferner, B.; Hoffmann, A. Tungsten foil laminate for structural divertor applications—Basics and outlook. *J. Nucl. Mater.* **2012**, *423*, 1–8. [[CrossRef](#)]
6. Monge, M.; Auger, M.; Leguey, T.; Ortega, Y.; Bolzoni, L.; Gordo, E.; Pareja, R. Characterization of novel W alloys produced by HIP. *J. Nucl. Mater.* **2009**, *386*, 613–617. [[CrossRef](#)]
7. Aguirre, M.V.; Martín, A.; Pastor, J.Y.; Llorca, J.; Monge, M.A.; Pareja, R. Mechanical properties of Y₂O₃-doped W–Ti alloys. *J. Nucl. Mater.* **2010**, *404*, 203–209. [[CrossRef](#)]
8. Loewenhoff, T.; Bardin, S.; Greuner, H.; Linke, J.; Maier, H.; Morgan, T.; Pintsuk, G.; Pitts, R.; Riccardi, B.; De Temmerman, G. Impact of combined transient plasma/heat loads on tungsten performance below and above recrystallization temperature. *Nucl. Fusion* **2015**, *55*, 123004. [[CrossRef](#)]
9. Pitts, R.; Carpentier, S.; Escourbiac, F.; Hirai, T.; Komarov, V.; Lisgo, S.; Kukushkin, A.; Loarte, A.; Merola, M.; Naik, A.S.; et al. A full tungsten divertor for ITER: Physics issues and design status. *J. Nucl. Mater.* **2013**, *438*, S48–S56. [[CrossRef](#)]
10. Norajitra, P.; Boccaccini, L.; Gervash, A.; Giniyatulin, R.; Holstein, N.; Ihli, T.; Janeschitz, G.; Krauss, W.; Kruessmann, R.; Kuznetsov, V.; et al. Development of a helium-cooled divertor: Material choice and technological studies. *J. Nucl. Mater.* **2007**, *367*, 1416–1421. [[CrossRef](#)]
11. Kurishita, H.; Kobayashi, S.; Nakai, K.; Ogawa, T.; Hasegawa, A.; Abe, K.; Arakawa, H.; Matsuo, S.; Takida, T.; Takebe, K.; et al. Development of ultra-fine grained W–(0.25–0.8) wt% TiC and its superior resistance to neutron and 3 MeV He-ion irradiations. *J. Nucl. Mater.* **2008**, *377*, 34–40. [[CrossRef](#)]
12. Kurishita, H.; Amano, Y.; Kobayashi, S.; Nakai, K.; Arakawa, H.; Hiraoka, Y.; Takida, T.; Takebe, K.; Matsui, H. Development of ultra-fine grained W–TiC and their mechanical properties for fusion applications. *J. Nucl. Mater.* **2007**, *367*, 1453–1457. [[CrossRef](#)]

13. Mutoh, Y.; Ichikawa, K.; Nagata, K.; Takeuchi, M. Effect of rhenium addition on fracture toughness of tungsten at elevated temperatures. *J. Mater. Sci.* **1995**, *30*, 770–775. [[CrossRef](#)]
14. Kim, Y.; Lee, K.H.; Kim, E.-P.; Cheong, D.-I.; Hong, S.H. Fabrication of high temperature oxides dispersion strengthened tungsten composites by spark plasma sintering process. *Int. J. Refract. Met. Hard Mater.* **2009**, *27*, 842–846. [[CrossRef](#)]
15. Rieth, M.; Dafferner, B. Limitations of W and W–1%La₂O₃ for use as structural materials. *J. Nucl. Mater.* **2005**, *342*, 20–25. [[CrossRef](#)]
16. Yar, M.; Wahlberg, S.; Bergqvist, H.; Salem, H.; Johnsson, M.; Muhammed, M. Spark plasma sintering of tungsten–yttrium oxide composites from chemically synthesized nanopowders and microstructural characterization. *J. Nucl. Mater.* **2011**, *412*, 227–232. [[CrossRef](#)]
17. Muñoz, A.; Monge, M.A.; Savoini, B.; Rabanal, M.E.; Garces, G.; Pareja, R. La₂O₃-reinforced W and W–V alloys produced by hot isostatic pressing. *J. Nucl. Mater.* **2011**, *417*, 508–511. [[CrossRef](#)]
18. Wesemann, I.; Spielmann, W.; Heel, P.; Hoffmann, A. Fracture strength and microstructure of ODS tungsten alloys. *Int. J. Refract. Met. Hard Mater.* **2010**, *28*, 687–691. [[CrossRef](#)]
19. Liu, R.; Xie, Z.; Fang, Q.; Zhang, T.; Wang, X.; Hao, T.; Liu, C.; Dai, Y. Nanostructured yttria dispersion-strengthened tungsten synthesized by sol–gel method. *J. Alloys Compd.* **2015**, *657*, 73–80. [[CrossRef](#)]
20. Liu, X.; Chen, J.; Lian, Y.; Wu, J.; Xu, Z.; Zhang, N.; Wang, Q.; Duan, X.; Wang, Z.; Zhong, J. Vacuum hot-pressed beryllium and TiC dispersion strengthened tungsten alloy developments for ITER and future fusion reactors. *J. Nucl. Mater.* **2013**, *442*, S309–S312. [[CrossRef](#)]
21. Xie, Z.M.; Liu, R.; Miao, S.; Yang, X.D.; Zhang, T.; Wang, X.P.; Fang, Q.F.; Liu, C.S.; Luo, G.N.; Lian, Y.Y.; et al. Extraordinary high ductility/strength of the interface designed bulk W–ZrC alloy plate at relatively low temperature. *Sci. Rep.* **2015**, *5*, 16014. [[CrossRef](#)] [[PubMed](#)]
22. Switzner, N.; Van Tyne, C.; Mataya, M. Effect of forging strain rate and deformation temperature on the mechanical properties of warm-worked 304 L stainless steel. *J. Mater. Process. Technol.* **2010**, *210*, 998–1007. [[CrossRef](#)]
23. Lian, Y.; Liu, X.; Feng, F.; Song, J.; Yan, B.; Wang, Y.; Wang, J.; Chen, J. Mechanical properties and thermal shock performance of W–Y₂O₃ composite prepared by high-energy-rate forging. *Phys. Scr.* **2017**, *T170*, 014044. [[CrossRef](#)]
24. Lian, Y.; Liu, X.; Xu, Z.; Song, J.; Yu, Y. Preparation and properties of CVD-W coated W/Cu FGM mock-ups. *Fusion Eng. Des.* **2013**, *88*, 1694–1698. [[CrossRef](#)]
25. Lian, Y.; Liu, X.; Cheng, Z.; Wang, J.; Song, J.; Yu, Y.; Chen, J. Thermal shock performance of CVD tungsten coating at elevated temperatures. *J. Nucl. Mater.* **2014**, *455*, 371–375. [[CrossRef](#)]
26. Xie, Z.; Liu, R.; Miao, S.; Zhang, T.; Wang, X.; Fang, Q.; Liu, C.; Luo, G. Effect of high temperature swaging and annealing on the mechanical properties and thermal conductivity of W–Y₂O₃. *J. Nucl. Mater.* **2015**, *464*, 193–199. [[CrossRef](#)]
27. Shen, T.; Dai, Y.; Lee, Y. Microstructure and tensile properties of tungsten at elevated temperatures. *J. Nucl. Mater.* **2016**, *468*, 348–354. [[CrossRef](#)]
28. Kurishita, H.; Arakawa, H.; Matsuo, S.; Sakamoto, T.; Kobayashi, S.; Nakai, K.; Pintsuk, G.; Linke, J.; Tsurekawa, S.; Yardley, V.; et al. Development of Nanostructured Tungsten Based Materials Resistant to Recrystallization and/or Radiation Induced Embrittlement. *Mater. Trans.* **2013**, *54*, 456–465. [[CrossRef](#)]
29. Wu, X.; Yang, M.; Yuan, F.; Wu, G.; Wei, Y.; Huang, X.; Zhu, Y. Heterogeneous lamella structure unites ultrafine-grain strength with coarse-grain ductility. *Proc. Natl. Acad. Sci. USA* **2015**, *112*, 14501–14505. [[CrossRef](#)]
30. Tanaka, K.; Mori, T. The hardening of crystals by non-deforming particles and fibres. *Acta Met.* **1970**, *18*, 931–941. [[CrossRef](#)]